Magnitude Image CSPAMM Reconstruction (MICSR)

[*]Moriel NessAiver, Ph.D. and [**]Jerry L. Prince, Ph.D.

[*]University of Maryland School of Medicine, Dept of Diagnostic Radiology
Baltimore, MD

[**]Johns Hopkins University, Dept of Computer and Electrical Engineering
Baltimore, MD

Corresponding Author:

Moriel NessAiver, Ph.D.

University of Maryland Medical School

Dept. of Diagnostic Radiology

22 S. Greene St.

Baltimore, MD 21201

410-706-8714 (office)

410-664-0196 (fax)

moriel@simplyphysics.com

Magnitude Image CSPAMM Reconstruction (MICSR)

Moriel NessAiver,[1] and [**]Jerry L. Prince[2]

Image reconstruction using complementary spatial modulation of magnetization, or CSPAMM, requires the subtraction of two complex datasets to remove the untagged signal. Although the resultant images typically have sharper and more persistent tags than images formed without complementary tagging pulses, handling the complex data is problematic and tag contrast still degrades significantly during diastole. This article presents a magnitude image CSPAMM reconstruction method called MICSR that is simple to implement and produces images with improved contrast and tag persistence. The MICSR method uses only magnitude images – i.e., no complex data – but yields tags with zero mean, sinusoidal profiles. A trinary display of MICSR images emphasizes their long tag persistence and demonstrates a novel way to visualize myocardial deformation. MICSR contrast and contrast-to-noise ratios were evaluated using simulations, a phantom, and two normal volunteers. Tag contrast 1000 msec after the R wave trigger was 3.0 times better with MICSR than with traditional CSPAMM reconstruction techniques while contrast-to-noise ratios were 2.0 times better.
Key words: magnetic resonance tagging, CSPAMM, HARP, myocardial motion

Since the introduction of myocardial tagging by Zerhouni et al. (1) in 1988 and spatial modulation of magnetization (SPAMM) by Axel et al. (2,3) in 1989, there have been many significant developments in the process of applying and analyzing tag patterns for visualization and quantification of motion and strain (4). Most tag tracking methods, both manual and automatic, work best with tag lines that have sharply-defined or "crisp" tag lines. Such patterns are produced by higher-order SPAMM (2) or DANTE (5) pulse sequences or by other selective k-space excitation pulse sequences (6). In k-space, these patterns are characterized by the presence of many spectral peaks: a strong peak at the first harmonic representing the tag frequency itself and additional peaks at integer multiples of the tag frequency, representing higher-order harmonics. Generally speaking, the higher the number of harmonic peaks generated and acquired, the better or sharper the tag line definition.

Harmonic phase (HARP) analysis was recently introduced as a rapid, robust, and automatic method to track motion and perform strain analysis in tagged

[1]University of Maryland School of Medicine, Dept of Diagnostic Radiology, Baltimore, Maryland

[2]Johns Hopkins University, Dept of Computer and Electrical Engineering, Baltimore, Maryland.

myocardial images (7,8). In contrast to other tag analysis approaches, HARP requires only the first harmonic in k-space, which corresponds to a tag pattern that is purely sinusoidal — i.e., not "crisp" at all. The introduction of HARP has resulted in a reexamination of optimal methods of producing tags (6), acquiring the image data (9), and producing the final motion and strain images (10). In this paper, we focus on the generation and reconstruction of sinusoidal tagged images. Their use might be for HARP analysis or, as we shall see, for a novel visualization of strain using a trinary display of the tagged images themselves.

A sinusoidal tag pattern can be produced using so-called 1-1 SPAMM pulse sequence (3), which consists of two equal RF pulses with a modulating gradient in-between; typically, the transverse magnetization is then "crushed." 1-1 SPAMM yields a longitudinal magnetization across the imaging plane that oscillates sinusoidally with a spatial frequency that is determined by the area of the modulating gradient. If the tip angle of each RF pulse is 45°, then the total tip angle of the tag pattern is 90°, and standard magnitude imaging methods yield a sinusoidal pattern. Since tags fade because of both longitudinal relaxation and imaging pulses, in order to increase tag persistence it is desirable to increase the tip angle of each RF pulse to 90°, which yields a total tag pattern tip angle of 180°. In this case, standard magnitude imaging yields a *rectified* tag pattern, which makes tag visualization problematic and tag analysis considerably more difficult because the mean of the sinusoidal pattern changes with tag fading. We note that although the use of complex image reconstruction can eliminate this rectification in principle, it is typically too time-consuming to perform the phase-corrections necessary to make this possible, especially when phased-array coils are used.

Complementary SPAMM (CSPAMM) (11,12) provides an elegant solution to the problem of tag fading and rectification. CSPAMM performs the imaging sequence twice, once using a [+90, +90] RF tag sequence and the other time using a [+90, -90] RF tag sequence. The tag pattern resulting from the second sequence is a sinusoid that is spatially shifted by one-half cycle. By subtracting these two complex images, the resulting sinusoidal tag pattern has a zero mean and peak-to-peak amplitude that is double that of either individual pattern. Since this process does

not alleviate the problem of phase variation across the FOV, it is still typically necessary to display the absolute value of the resulting images, which we denote by |CSPAMM|. In contrast to rectified SPAMM, |CSPAMM| images have "crisp" tags, corresponding to the zero-crossings of the subtraction image, which are stable with respect to tag fading. We note that when using multi-channel, phased-array coils, it is necessary to perform complex subtractions on the data from each coil separately and then combine these images using the square root of the sum of their squares.

It is apparent that while both 1-1 SPAMM and CSPAMM have *underlying* tag patterns that are sinusoidal, the use of magnitude images to avoid burdensome and problematic phase-corrections results in final tag patterns that are not sinusoidal. The basic goal of the research described herein was to develop a way to reconstruct zero-mean sinusoidal tag patterns using standard magnitude image reconstructions. There are several advantages to this strategy. First, all scanners produce magnitude reconstructions, while some scanners make it difficult to offload raw or complex data. Second, standard magnitude reconstructions are typically reconstructed using geometric corrections from calibration data, while raw or complex data are always uncalibrated. Third, this strategy avoids the need to both acquire phase calibration data and to apply phase correction algorithms, both problematic steps in acquisition and processing of MRI data.

In this paper, we have developed a *magnitude image CSPAMM reconstruction* (MICSR) process that reconstructs sinusoidal tag patterns using only magnitude images. Surprisingly, this method is very simple to implement and yields improved tag contrast and persistence. In the following sections, we first present the MICSR algorithm and compare its contrast behavior and contrast-to-noise ratio with that of CSPAMM and |CSPAMM|. We then discuss *k*-space imaging tradeoffs and describe our experimental methods. Our results include simulation, phantom, and normal volunteer results. We conclude with a discussion of these results.

THEORY
In this section, we first derive and compare the imaging equations for CSPAMM, |CSPAMM|, and MICSR. We then explore the noise properties of these methods and derive expressions for the contrast-to-noise ratios of the three methods. We conclude the section by considering alternative strategies for *k*-

space acquisition of the underlying data required for these methods. It should be noted that, in this section, we ignore the effects of the image pulses that occur throughout the longitudinal decay of the tag pattern. This effect will be studied in the Results section using both simulations and phantom imaging.

Imaging Equations
Let us assign the label 'A' to the series of images obtained using a [+90°, +90°] tagging pulse and assign the label 'B' to those obtained using [+90°, –90°]. Assuming that initially $M_Z(x) = M_0$ and that there is no motion, the spatial and temporal distribution of the Z magnetization after the tagging sequence can be described by the equations

$$A(x,t) = M_0 \left\{ 1 - \left[1 - \cos\left(\frac{2\pi x}{P} \right) \right] e^{-t/T_1} \right\} , \qquad [1]$$

$$B(x,t) = M_0 \left\{ 1 - \left[1 - \cos\left(\frac{2\pi x}{P} - \pi \right) \right] e^{-t/T_1} \right\} , \qquad [2]$$

where P is the spatial period of the tag pattern. We note that the tags in B are shifted by one half cycle (π radians) relative to those in A.

Subtracting Eq. [2] from Eq. [1] yields the standard CSPAMM image,

$$\begin{aligned} \text{CSPAMM} &= A - B \\ &= 2M_0 e^{-t/T_1} \cos(2\pi x/P), \end{aligned} \qquad [3]$$

where the second equation follows from straightforward algebra. We see that the underlying CSPAMM tag pattern is a zero-bias sinusoidal pattern with an initial amplitude equal to $2 M_0$ and an exponential decay in amplitude with time constant T_1. One potential difficulty with CSPAMM is that the signal subtraction in Eq. [3] must be done with complex data. This can be accomplished either in Fourier space using raw data or in image space after complex image reconstruction. The result, however, must either be phase-corrected so that the real component alone can be displayed or displayed as a magnitude image.

Taking the magnitude (complex modulus) of CSPAMM yields

$$\left| \text{CSPAMM} \right| = \left| A - B \right| = \left| 2M_0 e^{-t/T_1} \cos(2\pi x/P) \right| , \qquad [4]$$

which is the imaging equation for |CSPAMM|. Although the subtraction must still be a complex subtraction, underlying phase inhomogeneities are irrelevant in |CSPAMM| since they are removed by the modulus operator. We note that the tag pattern in a |CSPAMM| image is a *rectified sinusoid*, which has

one half the peak-to-peak amplitude of the original CSPAMM image.

MICSR requires only the magnitude images $|A|$ and $|B|$, yet like CSPAMM yields a zero-bias sinusoidal tag pattern. The MICSR reconstruction formula is given by

$$\text{MICSR} = |A|^2 - |B|^2. \qquad [5]$$

Using Eqs. [1] and [2], it is straightforward to show that

$$\text{MICSR} = 4M_0^2 \left(1 - e^{-t/T_1}\right) e^{-t/T_1} \cos(2\pi x / P), \qquad [6]$$

which shows that the tag pattern for MICSR is zero-bias sinusoidal, but the initial amplitude and temporal decay properties are different than that of CSPAMM.

Contrast Behavior

Let us define *tag contrast* as the peak-to-peak amplitude of the tag profile. This is equal to twice the amplitude of a pure sinusoid and is equal to the amplitude of a rectified sinusoid. Accordingly, tag contrast as a function of time for CSPAMM, |CSPAMM|, and MICSR can be derived from Eqs. [3], [4], and [6], yielding

$$\text{Contrast CSPAMM} = 4M_0 e^{-t/T_1}, \qquad [7]$$

$$\text{Contrast } |\text{CSPAMM}| = 2M_0 e^{-t/T_1}, \qquad [8]$$

$$\text{Contrast MICSR} = 8M_0^2\left(1 - e^{-t/T_1}\right)e^{-t/T_1}. \qquad [9]$$

The contrast of CSPAMM is clearly just twice that of |CSPAMM|; it should be viewed as a theoretical upper bound, however, because it is not easily achieved in practice. Our primary emphasis in this presentation is on a comparison between |CSPAMM| and MICSR, two CSPAMM reconstruction approaches readily achieved in practice.

Eqs. [7]–[9] are plotted in Fig. 1a assuming values of $M_0 = 1.0$ and $T_1 = 800$ msec. Plotted in Fig. 1b are the ratios of MICSR to CSPAMM| and |CSPAMM|

contrasts, given by

$$\frac{\text{MICSR Contrast}}{\text{CSPAMM Contrast}} = 8M_0\left(1 - e^{-t/T_1}\right) \qquad [10]$$

$$\frac{\text{MICSR Contrast}}{|\text{CSPAMM}| \text{ Contrast}} = 4M_0\left(1 - e^{-t/T_1}\right)\cdot \qquad [11]$$

We see from Fig. 1 that the CSPAMM and |CSPAMM| contrasts are quite different in character from MICSR. While the CSPAMM contrasts are largest at the outset, MICSR's contrast grows toward a peak value at around 500 ms after the tag application. On the other hand, the initial contrast of MICSR is very low, and we have found that this can produce inferior images in early systole. We now address this deficiency.

It is straightforward to show that MICSR can be written as

$$\text{MICSR} = \left(|A| - |B|\right) \times \left(|A| + |B|\right). \qquad [12]$$

During the period of low contrast, (roughly the first 100 msec), the term $|A| - |B|$ in Eq. [12] is very small, which in turn causes the MICSR contrast to be small. The MICSR equation can be modified by replacing this term with $\text{sign}(|A| - |B|)$ for t small, as follows:

$$\text{MICSR}' = \begin{cases} \text{sign}(|A| - |B|) \times (|A| + |B|) & t < 100\,\text{msec} \\ (|A| - |B|) \times (|A| + |B|) & t \geq 100\,\text{msec} \end{cases} \qquad [13]$$

A tag profile reconstructed using Eq. [13] is shown in Fig. 2. We see that when t is small, MICSR' is sinusoidal over a large portion of its period, but has an abrupt "zig-zag" at the zero-crossing of the sinusoid. Since the scale of this feature may be smaller than a pixel, for many applications this feature may be negligible. We now continue our theoretical analysis using MICSR; MICSR' is used in the results section.

The ratio of MICSR to CSPAMM and |CSPAMM| contrasts, given by Eqs. [10-11], contain the term M_0, which means that the relative contrast is dependent on
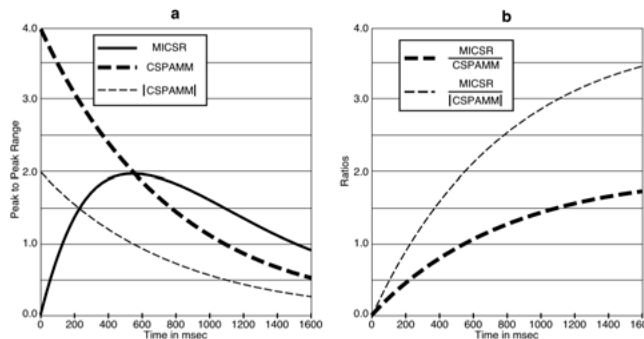

FIG. 2. **a:** Theoretical peak-to-peak signal range as a function of time for CSPAMM, |CSPAMM| and MICSR. These curves assume a value of 1.0 for M_0 and a value of 800 msec for T1. **b:** The ratio of MICSR to CSPAMM and MICSR to |CSPAMM|.
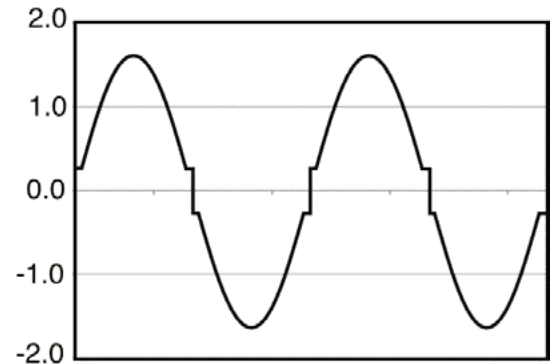

FIG. 1. MICSR' tag profile using $\text{sign}(|A| - |B|) \times (|A| + |B|)$.

the underlying magnetization. What really matters in imaging, however, is not whether the underlying contrast alone is improved (which after all can be done using a simple gain factor) but whether the contrast-to-noise is improved. Accordingly, we now compare the noise behavior of these three methods.

Contrast-to-Noise Behavior

The most common way to measure noise in an MR image is to use a region-of-interest in the background – i.e., the air – to determine the underlying noise variance. Contrast-to-noise (CNR) is usually computed using this background noise. In our case, however, since both |CSPAMM| and MICSR are computed as nonlinear functions of the underlying image signal, it is necessary to use the noise *within* the object being imaged in computing CNR. Also, since the noise power will depend on the signal intensity of the object, the presence of an imposed tag pattern causes the contrast-to-noise ratio (CNR) to vary both spatially and temporally. To understand the nature of the temporal and spatial variation of CNR, yet to also retain some simplicity, we have elected to compute the temporal evolution of CNR at the two signal extremes – i.e., the peaks and the zero-crossings (tags) of the tag pattern.

Assume that the noise in each of the real and imaginary channels of the complex images A and B are independent Gaussian random variables, each with mean zero and variance σ^2. If one were able to accurately perform phase corrections on A and B, then the noise in the real-valued CSPAMM image, $A - B$, would have a zero mean and variance of $2\sigma^2$. In this case, the contrast is twice the amplitude given in Eq. [3], the noise standard deviation is $\sqrt{2}\sigma$, and the CNR is therefore

$$\text{CNR CSPAMM} = \frac{4 M_0 e^{-t/T_1}}{\sqrt{2}\,\sigma} = \frac{\sqrt{8}\,M_0 e^{-t/T_1}}{\sigma}, \qquad [14]$$

which is spatially invariant and exponentially decaying with time..

It has been previously shown that image intensities in magnitude MRI images follow a Rician distribution (14). When the signal-to-noise ratio in such an image exceeds 3.0, however, the noise approaches an additive Gaussian random variable with a variance equal to that of the underlying image. Therefore, in |CSPAMM| where the underlying image is $A - B$, the noise variance in the high signal regions (e.g., between the tag lines) is $2\sigma^2$, just like in CSPAMM. The situation changes, however, at the zero-crossings – i.e., the tags – of the CSPAMM

image. Here, the underlying image value is zero, and the Rician distribution becomes a Rayleigh distribution with mean and variance given by

$$\text{Mean } |\text{CSPAMM}|_{(\text{tag})} = 2\sigma^2 \sqrt{\pi/2}, \qquad [15]$$
$$\text{Variance } |\text{CSPAMM}|_{(\text{tag})} = \sigma^2(4-\pi).$$

Note that this is twice the mean and variance usually written for the Rayleigh random variable in the background of an MR image (13), because in this case the underlying image is $A - B$, which has twice the variance of a single image. Interestingly, we find that the mean of |CSPAMM| is *not* zero; therefore, the expected contrast of |CSPAMM| is actually reduced because of noise.

Using the variance given in Eq. [15], and incorporating the reduction in expected contrast, the CNR of |CSPAMM| images at the peak signal regions is given by

$$\text{CNR } |\text{CSPAMM}|_{(\text{peak})} = \frac{2 M_0 e^{-t/T_1} - 2\sigma^2 \sqrt{\pi/2}}{\sqrt{2}\,\sigma} \qquad [16]$$

and the CNR at the tag lines is given by

$$\text{CNR } |\text{CSPAMM}|_{(\text{tags})} = \frac{2 M_0 e^{-t/T_1} - 2\sigma^2 \sqrt{\pi/2}}{\sigma\,\sqrt{4-\pi}} \qquad [17]$$

We note that the ratio of the |CSPAMM| CNR at the tag lines to that at the peak is $\sqrt{2/(4-\pi)} \approx 1.526$, which clearly reveals the spatially-varying nature of CNR in |CSPAMM| images.

To calculate the noise behavior of MICSR, we use the equation $\text{MICSR} = |A|^2 - |B|^2$, given in Eq. [6]. Let the noise-free signal in A be denoted by $\overline{A}$. The complex MRI image is given by

$$A = \overline{A}\cos\phi + n_c + j(\overline{A}\sin\phi + n_s)\,, \qquad [18]$$

where ϕ is an unknown phase angle (which may be random and/or spatially varying) and n_c and n_s are independent, zero-mean, Gaussian random variables each with variance σ^2. It is straightforward to show that

$$\text{Mean } |A|^2 = \overline{A}^2 + 2\sigma^2, \qquad [19]$$
$$\text{Variance } |A|^2 = 4\overline{A}^2\sigma^2 + 4\sigma^4.$$

Analogous expressions to those in Eqs. [18] and [19] hold for the complementary image B, and since the noise terms in A and B are independent, it follows that

$$\text{Mean MICSR} = \overline{A}^2 - \overline{B}^2, \qquad [20]$$
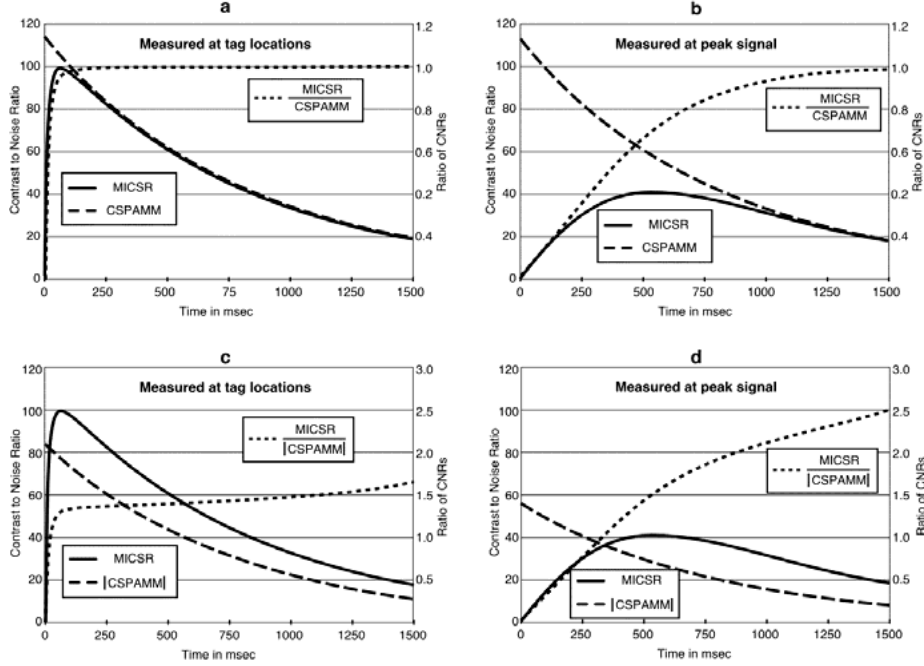$$\text{Variance MICSR} = 4\sigma^2\left(\overline{A}^2 + \overline{B}^2\right) + 8\sigma^4.$$

FIG. 3. Theoretical Contrast-to-Noise Ratios of CSPAMM and |CSPAMM| vs. MICSR assuming underlying Signal-to-Noise Ratio of 40. The Y-axis on the left is the CNR while the Y-axis on the right is the ratio of MICSR to CSPAMM or |CSPAMM| a: CSPAMM vs MICSR with noise measured at tag locations (Zero crossings.) b: CSPAMM vs MICSR with noise measured at location of peak signal.   c: |CSPAMM| vs MICSR with noise measured at tag locations (Zero crossings.) d: |CSPAMM| vs MICSR with noise measured at location of peak signal.

Unlike that of |CSPAMM|, the variance of MICSR images is highly dependent on the spatial and temporal variations of both A and B. We now examine the temporal variation of MICSR CNR at the both the zero-crossings – i.e., the tags – and the signal peaks.

Spatially, the peak MICSR signal is produced when $A = M_0$ and $B = M_0\left(1 - 2e^{-t/T_1}\right)$. At the location of the peak signal, where $A \gg \sigma$, we can neglect the $8\sigma^4$ term in the variance of Eq. [20]. Dividing Eq. [9] by the square root of the variance in Eq. [20] and substituting the above values for A and B yields the contrast-to-noise ratio of MICSR at the peak

$$\text{CNR MICSR}_{(peak)} = \frac{4M_0}{\sigma} \frac{\left(1 - e^{-t/T_1}\right)e^{-t/T_1}}{\sqrt{1 + (1 - 2e^{-t/T_1})^2}} . \qquad [21]$$

At a zero crossing, we know that $A = B$ for all time. Therefore, the MICSR variance becomes $8\sigma^2\left(\overline{A}^2 + \sigma^2\right)$. Dividing Eq. [9] by the square root of this variance and substituting $A = M_0\left(1 - e^{-t/T_1}\right)$ yields the CNR of MICSR at the zero crossings

$$\text{CNR MICSR}_{(tag)} = \frac{\sqrt{8}M_0^2\left(1 - e^{-t/T_1}\right)e^{-t/T_1}}{\sigma\sqrt{M_0^2\left(1 - e^{-t/T_1}\right)^2 + \sigma^2}} . \qquad [22]$$

When $A > 3\sigma$, (which typically occurs in when t > 60 msec), we can ignore the σ^2 term in the denominator and Eq. [22] can be simplified to

$$\text{CNR MICSR}_{(tag)} = \frac{\sqrt{8}\,M_0\,e^{-t/T_1}}{\sigma} , \qquad [23]$$

which is identical to the CNR of the phase corrected CSPAMM given in Eq. [14].

The CNR's for CSPAMM, |CSPAMM|, and MICSR together with their CNR ratios are plotted in Fig. 3. We can see from Fig. 3a that the CNR of MICSR at the tag locations is nearly identical to that of (phase-corrected) CSPAMM once t is greater than roughly 60 msec. From Fig. 3c we see that it is 30–60% better than that of |CSPAMM|. Because the noise in MICSR is heavily dependent on the signal amplitude, when measuring the noise at the location of the absolute signal peaks, the CNR of MICSR only approaches that of CSPAMM when $t > 1000$ msec. However, it exceeds that of |CSPAMM| after roughly 300 msec, and the ratio exceeds 2 when $t > 900$ msec. This substantiates (at least theoretically) our claim that MICSR should have better tag persistence than |CSPAMM|, and should also have superior visualization of motion through the diastolic phase in tagged cardiac MRI.

k-Space Considerations

Immediately after applying a [+90,+90] or [+90,-90] tag, the average M_Z and hence the average signal in a complex image acquired at that time is zero. This appears as little or no signal near the center of *k*-space. Instead, most of the signal power is located at the +/- peaks corresponding to the spatial frequency of the tags. As an example, when using a sinusoidal pattern with a 6 mm period over a 280 mm FOV there will be a total of 280/6 = 46.7 cycles across the FOV.
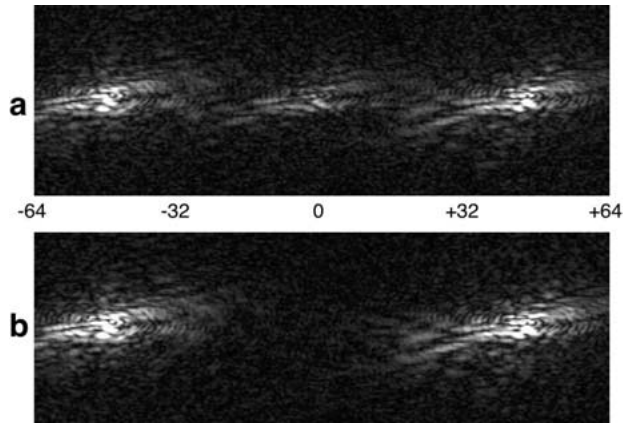
FIG. 4. *K*-space data from the second volunteer's scan (scan parameters given in table 1). Trigger delay of 110msec, 32x128 matrix, centered acquisition, tag peaks located at ± 47. The numbers represent the *k*x coordinate. **(a)** Absolute value of *k*-space data with [+90, +90] tagging and a trigger delay of 30 msec. **(b)** Subtraction of data from [+90, +90] and [-90,+90] tagging sequences.

This will produce large peaks in *k*-space at roughly ± 47 points from the center.

Fig. 4a shows an example set of *k*-space data acquired with a trigger delay of 30 msec. With this trigger delay, the peak at the center of *k*-space is fairly small. As M_Z begins to recover, this peak will begin to grow while the tag peaks will decrease in amplitude. However, after performing the subtractions that are part of both CSPAMM and MICSR, the signal at the center drops out completely and the signal power is split between the two tag peaks as shown in Fig. 4b.

The presence of two large peaks has significant implications when designing an imaging sequence. It is common practice to use a fractional echo sequence when acquiring cardiac cine images in order to shorten the TE thereby minimizing motion related dephasing. Using a fractional echo that captures only one of the two tag peaks would throw away almost half the signal, thereby reducing the SNR by $\sqrt{2}$. For this reason, when implementing a tagged imaging sequence, a centered echo data acquisition should be used. Additionally, when using a sinusoidal tag profile, there are no higher harmonics and therefore it is only necessary to use a matrix size that will adequately sample the two tag peaks seen in Fig. 4.

The reduced matrix size is adequate for MICSR reconstruction; however, care needs to be taken when producing |CSPAMM| images from the same data. The problem with |CSPAMM| reconstruction can be understood by realizing that rectified sinusoids have significantly higher frequency components caused by the nonlinear absolute-value operator. These components include a doubling of the fundamental frequency and the introduction of higher-order harmonics. Without adequate zero padding, the resulting harmonic series will be truncated resulting in tag blurring and corresponding reduction of tag contrast.

METHODS
MR Imaging
All scans were performed on a Marconi 1.5T Eclipse. The CSPAMM tagging pulse sequence consisted of two non-selective, 90°, 400 μsec RF pulses with an intervening 700 μsec modulating gradient. The tag profile is shifted half a period by phase alternating the second pulse by 180°. Three different versions of a RF-FAST (spoiled gradient echo) cine imaging sequence were used with the scan parameters listed in Table 1. In all sequences, the tag lines were oriented perpendicular to the frequency encode gradient.

The phantom consisted of four long, thin cylinders inside a larger cylinder, similar in size to a common head coil phantom. The thin cylinders were doped to have different T_1 and T_2 values. All measurements were made in the cylinder with T_1/T_2 values of 800/45, closest to myocardium. The phantom imaging was performed using a quadrature head coil. Two sets of phantom images were obtained. The first set used a tag cycle of 8 mm with a FOV of 250 mm and 256 point readout matrix, parameters similar to those often used in cardiac imaging. This provides close to 8 points per tag cycle or 4 points per zero crossing and is used to demonstrate the differences in typical |CSPAMM| and MICSR tag profiles. The second set was acquired twice using a tag cycle of 28 mm and a FOV of 280 mm resulting in 25.6 points per tag cycle. By subtracting these images it is possible to make noise measurements near the zero crossings and near the signal peaks.

After obtaining informed consent, both volunteers were imaged with a 4-channel cardiac phased-array coil. A total of four breath-holds were required, two with phase alternated tags in one direction and two with phase and frequency directions swapped. A grid pattern was obtained by multiplying together the results from the MICSR processing of the orthogonally tagged images. Prior to reconstruction of the second volunteer's images, the data was zero-filled and interpolated to a 512x512 matrix.

In the Theory section, we derived theoretical contrast behavior as a function of time while ignoring the RF pulses that are part of an imaging sequence. In order to predict the results of an actual imaging

experiment, an Excel spreadsheet was used to simulate the time course of the M_Z magnetization and signal intensities. The scan parameters used in the simulation were the same as those listed in Table 1 for the phantom imaging experiment. We assumed a T_1 value of 800 msec.

Trinary Image Display

The preceding analysis reveals excellent MICSR CNR at the tag locations throughout the entire cardiac cycle, rivaling that of CSPAMM itself. On the other hand, MICSR CNR at peak locations is generally poor in systole, and does not approach that of |CSPAMM| until $t > 300$ ms and CSPAMM until $t > 900$ ms. These properties of MICSR suggest the use of a nonlinear transformation of the MICSR intensities for visualization purposes that focuses attention on the tag locations while downplaying the peak intensities. There are an infinite number of transformations that satisfy these basic principles. We have developed the following mapping, which we refer to as the *MICSR trinary visualization*.

Unlike |CSPAMM| images, MICSR images have both positive and negative values. In particular, their zero-crossings represent the tag locations. In order to "see" the MICSR image values around the tags, we maintain a linear relationship between these values and the visualized intensities. However, in our trinary visualization, MICSR values that are larger in magnitude are thresholded and displayed as constant. Accordingly, the MICSR trinary mapping is given by

$$TrinaryMap = \begin{cases} +1, & MICSR \geq \varepsilon \\ \dfrac{MICSR}{\varepsilon}, & |MICSR| < \varepsilon \\ -1, & MICSR \leq \varepsilon \end{cases} \quad [27]$$

where ε is a small positive number. A plot showing the relationship between the trinary mapping and MICSR image values is shown in Fig. 5.
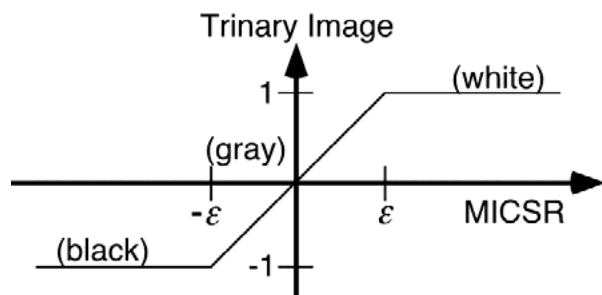

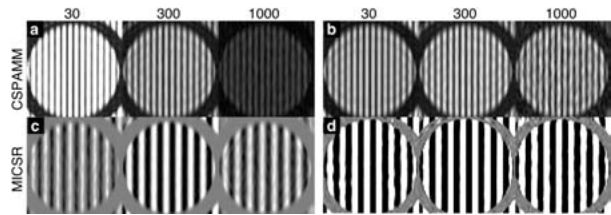
FIG. 5. Mapping of MICSR values into trinary image.

FIG. 6. MICSR and and |CSPAMM| images of cylinder with T1 of 800 msec at trigger delays of 30, 300 and 1000. **(a)** |CSPAMM| images with constant window and level settings demon-strating the change in contrast over time. **(b)** |CSPAMM| images with window and level set differently for each image. **(c)** MICSR images with broad ε. **(d)** MICSR images with narrow ε.

The choice of ε is important in determining the overall appearance and utility of the trinary display. If selected too large, then a fair amount of the image is dominated by a grayscale MICSR image and the constant intensity regions are diminished. If selected too small, then the transition regions between "white" and "black" bands are very narrow and are subject to noise. There are several sensible possibilities for selection of ε. Although there may be more principled ways to select ε, to date we select a constant value that provides a pleasant appearance throughout all images in a cine series.

RESULTS

In this section, we present data from |CSPAMM| and MICSR reconstructions only since we do not have the software to calculate and apply the phase corrections necessary for CSPAMM.

Phantom Images

Fig. 6 shows three representative pairs of images from the first phantom series, with trigger delays of 30, 300, and 1000 msec. The |CSPAMM| images in Fig. 6a were filmed with fixed window and level settings and clearly demonstrate how the contrast changes over time. The same images are shown in Fig. 6b with individualized settings to produce images with similar apparent contrast. This is easy to do for a few images but difficult when there are 16 to 30 images that comprise a cine series.

In Fig. 6c, a large value was chosen for ε while a much smaller value was chosen for the images in Fig 6d. The MICSR images in Fig. 6d highlight the advantage of tagged regions that alternate between positive and negative, regardless of the absolute amplitude. This effectively divides the images into three regions; tissue will always be black or white while the background (air) will be near zero. With this type of trinary display, even though the actual contrast is changing over time, the displayed contrast
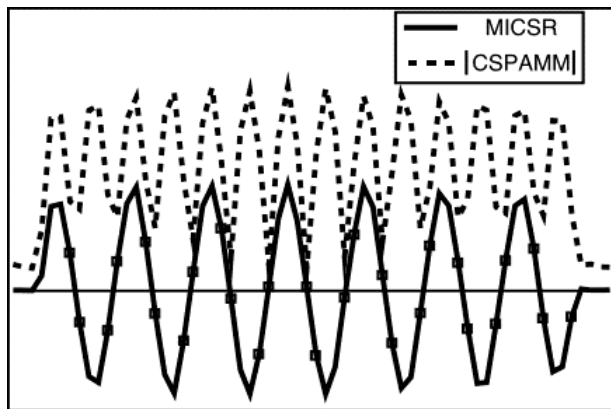
FIG. 7. Measured MICSR and |CSPAMM| tag profiles at a trigger delay of 300. The squares on the MICSR curve are the location of sampled points that bracket a zero crossing.

remains constant except for some small fluctuations in the edges during periods of low SNR.

Tag Profile.   Fig. 7 displays the tag profiles obtained from the images in Fig. 6 at a trigger delay of 300 msec. Note that the amplitude (depth) of each trough of the |CSPAMM| data varies across the FOV. As was discussed under *k*-space considerations, inadequate zero-filling will result in a poor representation of the tag profile. In this case, we used a tag cycle of 8 mm over a FOV of 250 mm. This produced primary peaks in *k*-space at ±31.25, (250/8). After taking the absolute value, the peaks moved to ±62.5 with the first harmonics at ±125. With a readout matrix of 256 points, these harmonic peaks were only partially sampled and no higher harmonics were included at all. Zero-padding the matrix prior to the Fourier transform can improve the |CSPAMM| tag profile; however, even with zero-padding to a 1024 matrix (not shown), every fourth tag line is still poorly represented.

As can be clearly seen in Fig. 7, the MICSR data retains its sinusoidal shape even when sparsely sampled. Very good estimates of the zero crossings can easily be obtained by linear interpolation between

pairs of points, (the squares in Fig. 7), bracketing the zero crossings. The largest errors in the |CSPAMM| tags occur when the MICSR points are equidistant on either side of the zero crossing.

Effect of Imaging Sequence on Contrast. **A**s was discussed in the Theory section, |CSPAMM| contrast is proportional to M_0 while MICSR contrast is proportional to M_0^2. This results in MICSR images having a peak-to-peak range that is two to three orders of magnitude larger than |CSPAMM| images making it difficult to compare results. One approach to facilitate comparison would be to eliminate the M_0 term completely by dividing the unsubtracted source images, *A* and *B*, by M_0, effectively setting M_0 to 1 as was done in the theory section. In an actual imaging experiment, the true value for M_0 is not known. It is reasonable to assume, however, that M_0 is proportional to the measured peak signal in the source (unsubtracted) images at the beginning of the cardiac cycle. Therefore, we determine the maximum absolute signal in an area of interest and then normalize all images in the cine sequence prior to the final reconstruction steps for both |CSPAMM| and MICSR.

The simulated time courses of the peak-to-peak signal for |CSPAMM| and MICSR for three heartbeats are shown in Fig. 8. Note that the time course for the first heartbeat is significantly different (higher) than for the subsequent beats which have been driven to a pseudo steady state. Because of this dramatic signal change from the first to subsequent heartbeats, we always use a stabilization or "throwaway" beat, and have therefore chosen to normalize the data to the peak signal in the source images at the start of the second beat.

Fig. 9 depicts the measured, normalized, peak-to-peak signal from the second phantom imaging sequence. The general shapes of the measured curves agree well with the predicted curves. The measured MICSR curve is actually flatter than that predicted resulting in
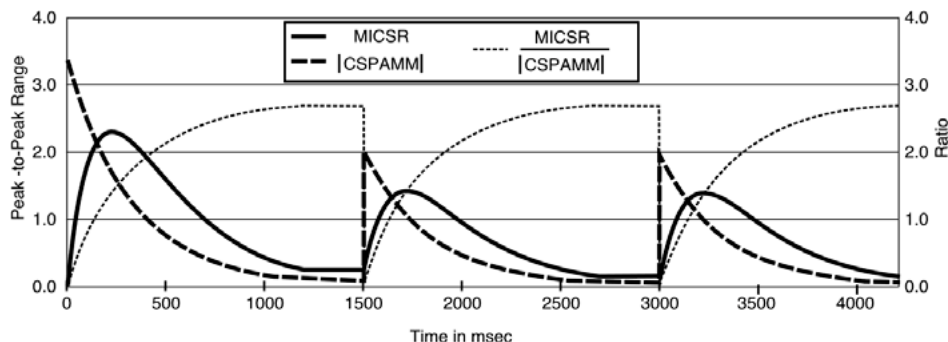

FIG. 8. Simulated 3 heartbeat approach to pseudo steady-state of peak-to-peak signal during the imaging sequence used in the phantom study. Assumed parameters: T1=800, TR= 8.55 msec, Flip=10°, R-R interval=1500 msec, Imaging time=1200 msec, recovery time=300 msec
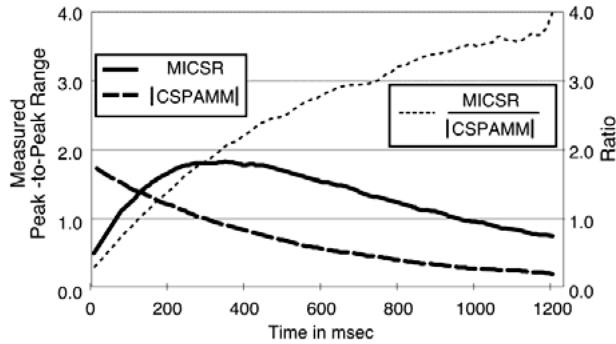
FIG. 9. Peak-to-peak signal values in a phantom after |CSPAMM| or MICSR processing. Parameters: T1=800, TR=8.55, Flip=10°, R-R interval=1500 msec, Imaging window=1200 msec, recovery time=300 msec. Data was normalized by dividing by the peak signal in the first image in the series.
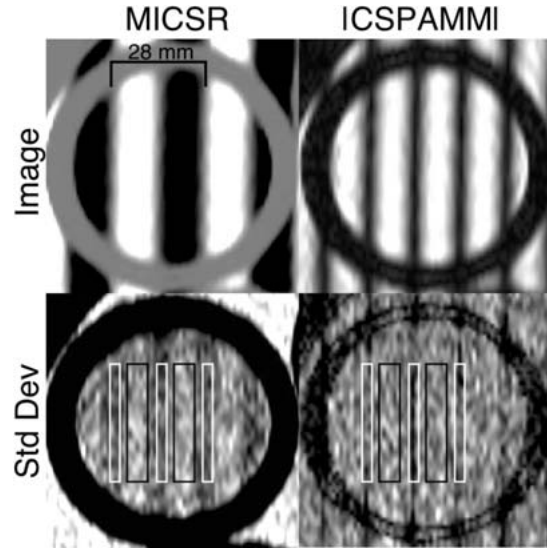

FIG. 10. Example MICSR and |CSPAMM| images from phantom study with 28 mm tag cycle. The lower two images display the standard deviation of each pixel across the 69 frame cine. When calculating peak and tag CNR for each image, the noise at the peaks was estimated inside of black boxes (7 mm wide each) and noise at the tags was estimated inside of the white boxes (1.4 mm wide each).

a higher than expected ratio between the two techniques. The change in the MICSR curve seems to be due to raising the ends as opposed to lowering the middle. One possible explanation relates to the RF pulse. The simulation assumes a perfectly square 10° RF pulse while the actual imaging sequence used a Gaussian RF pulse. Initial, simple simulations seem to support the hypothesis that the RF pulse is responsible for the flattening, but a more detailed simulation should be undertaken for definitive proof.

Contrast-to-noise Ratio Over Time. The second series of phantom images, with a tag cycle of 28mm, was acquired twice. Subtracting these repeated series eliminates the signal, leaving the noise present throughout the FOV. The noise at the tag locations was estimated by measuring the standard deviation at the zero crossings ± 2.5% of the tag cycle as depicted by the white boxes shown in Fig. 10, each having a width of 1.4 mm. The noise at the signal peaks was estimated by measuring the standard deviation at the peak ± 12.5% of the tag cycle as depicted by the

black boxes, each having a width of 7 mm. The resulting CNR values as a function of time are plotted in Fig. 11. These measured results agree very well the theoretical results given in Fig. 3. The most significant deviation from the theoretical values is a slightly lower |CSPAMM| CNR at the tag locations. The region where the theoretical |MICSR| noise is low is very narrow. Estimating the noise too far from the actual tag location will result in a larger apparent standard deviation thereby lowering the CNR curve. This underestimation of the |CSPAMM| CNR also results in the measured ratio between MICSR and |CSPAMM| being slightly higher than theoretical predictions.
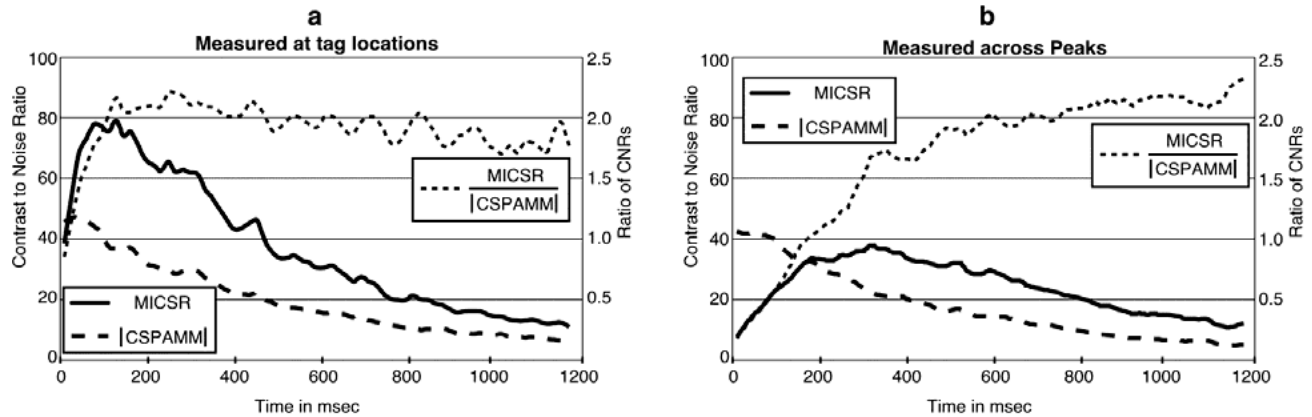

FIG. 11. Contrast-to-Noise ratios measured using |CSPAMM| and MICSR. **(a)** Noise measured at tag locations ±2.5% of tag cycle. **(b)** Noise measured at signal peak ±12.5% of tag cycle.
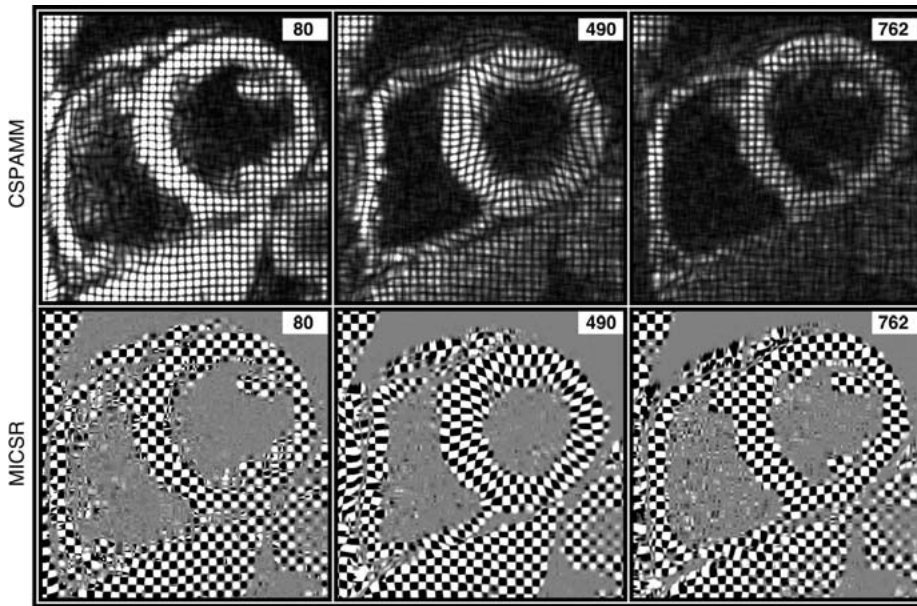
FIG. 12. Representative CSPAMM and MICSR images from Volunteer #1. Trigger delays of 80, 490 and 762 correspond to early systole, early diastole and late diastole.

Volunteer #1

The goal of the first volunteer imaging sequence was to obtain one short axis slice with good spatial resolution and adequate temporal resolution to demonstrate the feasibility of the technique. Fig. 12 shows three representative pairs of images from volunteer #1. Both reconstruction methods show good tag definition throughout the cardiac cycle. However, the |CSPAMM| images demonstrate a wide range of contrasts between the tag lines and interspersed tissue both within a single image and between images while the trinary windowing of the MICSR images provides a consistent, easily recognizable contrast throughout the cardiac cycle.

The MICSR image obtained at a trigger delay of 80 msec was reconstructed using the alternate version of the MICSR equation, $\mathrm{sign}(|A|-|B|)\times(|A|+|B|)$. Note the existence of imperfections in the grid pattern at the edge of the myocardium. One requirement of any subtraction technique is that the images be precisely aligned. A slight misregistration at the zero crossings of the tag pattern may result in the term $(|A|-|B|)$ changing sign. When using the normal MICSR equation, the magnitude of the difference is usually small resulting in the product $(|A|-|B|)\times(|A|+|B|)$ being small and any error is of little notice. When using the modified MICSR equation, a change in the sign of the difference will have a much greater effect. The images shown in Fig. 12 were obtained over four breath-holds, increasing the chance for misregistration. A redesign of the imaging sequence that would allow all four required sets of images to be acquired in a single breath-hold would significantly reduce this artifact.

Volunteer #2

The images from Volunteer #1 required four 21-second breath-holds and resulted in images at only a single anatomical location. A faster cine sequence was used with Volunteer #2. In Fig. 13 we show end-systolic images from four separate anatomic locations each being part of a 16-frame cine. Total time for all four slices was only four 13-second breath-holds, less total scan time than the single slice from volunteer #1 yet with similar image quality. Note that areas of high strain are easy to identify as a distortion in the grid pattern. Where the direction of strain is
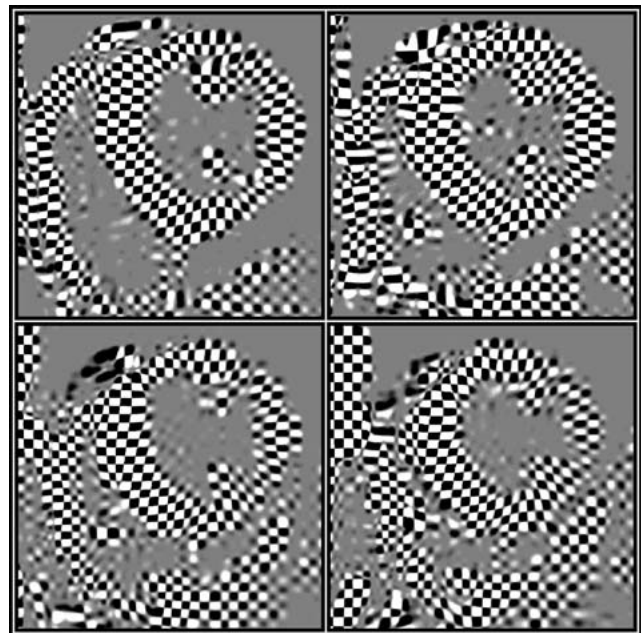

FIG. 13. End systolic MICSR images from four contiguous slices from volunteer #2. All images required to reconstruct 16 images at four slices were acquired in four 13-second breath holds.

perpendicular to the grid pattern, a square distorts into a rectangle. Where the direction of strain is at an angle, the grid square becomes a diamond. Because of the tight trinary windowing (small ε) there is no broadening of the tag lines as is common in SPAMM and CSPAMM images, particularly in late diastole.

Due to a difficulty in saving the raw data at the data rates used, we were unable to reconstruct the corresponding |CSPAMM| images for comparison.

DISCUSSION

We have presented a simple method of using magnitude images to reconstruct images from CSPAMM data. The MICSR method has several advantages over more traditional reconstruction methods. They are: 1) The scanner's recon system can be used to perform the initial magnitude reconstructions, performing all coil combination, gradient correction, and surface coil correction (if desired.) 2) The final reconstruction step $\left(|A|^2 - |B|^2\right)$ produces true sinusoidal tag profiles as opposed to rectified sinusoids. 3) The images can be displayed with 'trinary' window and level settings providing consistent apparent contrast throughout the cardiac cycle. 4) Accurate information of the zero crossings, corresponding to the tag lines in normal |CSPAMM| reconstruction, can be obtained/retained without the need for large-scale interpolation. 5) Peak MICSR contrast and CNR is obtained between 200 and 500 msec after the R-wave trigger corresponding to late systole to early diastole; the point in the cardiac cycle exhibiting the largest myocardial deformation. 6) Useful tag contrast persists at higher levels and for a longer period of time. 7) MISCR contrast-to-noise at the actual tag locations is nearly equal to phase corrected CSPAMM throughout all but the first 50 msec of the cardiac cycle and is 30 to 50% greater than |CSPAMM|. 8) The improvement between MICSR and |CSPAMM| continues to improve even to the end of the cardiac cycle.

The most significant advantage of the MICSR technique is that the final images are zero-mean sinusoids. The usual dark tag lines that fade over time have been replaced by positive/negative transitions. The slope of the tagging pattern is sharpest at these zero crossings. Tight thresholding creates a trinary display with visual contrast that remains constant throughout the cardiac cycle. While watching cine loops of typical SPAMM and CSPAMM images, one tends to track the motion of lines. With MICSR images, one is more readily able to identify a small region, a single 3.5 mm x 3.5 mm square for example, and watch how it moves and deforms throughout the cardiac cycle. Although in this paper we make no attempt to quantify the strain, it is obvious that the MICSR images would be ideal for strain analysis. Because of the ease of identifying edges (zero crossings) the analysis can be done using common tag tracking type processing.

In addition to these demonstrated advantages, MICSR images are also optimized, in theory, for processing using HARP. Because the tagging is sinusoidal with a zero mean, the Fourier transform will consist primarily of two peaks, at the plus and minus frequency of the tags. There will be little or no contamination from signal at low frequencies, (DC component), nor will there be higher-order harmonics. This holds true throughout the cardiac cycle whereas with SPAMM and CSPAMM, the contribution from low frequencies and higher harmonics change as a result of M_Z recovery. Demonstrating these advantages for HARP analysis will be the subject of further research.

The goal of the second volunteer imaging sequence was to cut the total scan time down while maintaining adequate spatial and temporal resolution. This was accomplished by increasing the bandwidth, reducing the matrix size and increasing the phase encode group (PEG) size. These changes resulted in a four-fold improvement in scan time while also improving temporal resolution making it possible to acquire one tag orientation for four slices in a single breath-hold and all four orientations for four slices in four breath-holds. We intend to implement a scan sequence that will acquire all four tag orientations for a single slice in a single 16 to 20 heart beat breath-hold eliminating the potential problem of respiratory related misregistration. Within 10 breath-holds, it will be possible to acquire MICSR grid images covering the whole heart. In addition to the strain analysis, this type of data set should facilitate measuring cardiac mass, left and right ventricular volumes, and stroke volumes.

It is well known that the RF pulses of the imaging sequence have significant effect on tag persistence (15,16). It is possible to improve SPAMM and CSPAMM tag persistence (contrast) by starting with a small flip angle when M_Z is large and increasing the flip angle as M_Z decreases (15,16). Although we do not currently have the ability to use variable flip angles in cardiac gated cine imaging on our Marconi 1.5T Eclipse, we will be performing simulations to examine the effect of variable flip angles on MICSR

contrast. In addition, we will be exploring the optimizations that might be possible with different imaging sequences such as multi-shot EPI or spiral EPI.

Because of the spatial and temporal differences in contrast and contrast-to-noise, comparisons between CSPAMM, |CSPAMM|, and MICSR cannot be absolute. One method cannot be claimed to be superior to the other in all respects. For example, it is clear from all standpoints that |CSPAMM| has better contrast and CNR than MICSR immediately after tag application. So, it might be reasonable to use |CSPAMM| if early systolic imaging were the goal. On the other hand, |CSPAMM| does not produce a sinusoidal pattern, and this might be problematic if, for example, HARP processing were going to be used. Further, since tag tracking is the usual objective when |CSPAMM| is used, we can see from Fig. 11a that MICSR has superior CNR after a very short interval at the location of the tags, which would then point to MICSR even in this application. If, on the other hand, diastolic imaging is the goal, then MICSR stands up well from all viewpoints, even in comparison to CSPAMM itself.

ACKNOWLEDGEMENTS

REFERENCES

1. Zerhouni, EA, Parish, DM, Rogers, WJ, Yang, A, Shapiro, EP. Human heart: tagging with MR imaging--a method for noninvasive assessment of myocardial motion. Radiology 1988; 169: 59-63.
2. Axel, L, Dougherty, L. Heart wall motion: improved method of spatial modulation of magnetization for MR imaging. Radiology 1989; 172: 349-50.
3. Axel, L, Dougherty, L. MR imaging of motion with spatial modulation of magnetization. Radiology 1989; 171: 841-5.
4. Amini, AA, Prince, JL. Measurement of cardiac deformations from MRI : physical and mathematical models. Boston: Kluwer Academic Publishers, 2001.
5. Mosher, TJ, Smith, MB. A DANTE tagging sequence for the evaluation of translational sample motion. Magn Reson Med 1990; 15: 334-9.
6. Kerwin, WS, Prince, JL. A k-space analysis of MR tagging. J Magn Reson 2000; 142: 313-22.
7. Osman, NF, Kerwin, WS, McVeigh, ER, Prince, JL. Cardiac motion tracking using CINE harmonic phase (HARP) magnetic resonance imaging. Magn Reson Med 1999; 42: 1048-60.
8. Osman, NF, McVeigh, ER, Prince, JL. Imaging heart motion using harmonic phase MRI. IEEE Trans Med Imaging 2000; 19: 186-202.
9. Sampath, S, Derbyshire, JA, Osman, NF, Atalar, E, Prince, JL. Real-Time Imaging of Two-dimensional Cardiac Strain Using a FastHARP Pulse Sequence. Magn Reson Imaging 2002; In Revision.
10. Osman, NF, Prince, JL. Visualizing myocardial function using HARP MRI. Phys Med Biol 2000; 45: 1665-82.
11. Fischer, SE, McKinnon, GC, Maier, SE, Boesiger, P. Improved myocardial tagging contrast. Magn Reson Med 1993; 30: 191-200.
12. Fischer, SE, McKinnon, GC, Scheidegger, MB, Prins, W, Meier, D, Boesiger, P. True myocardial motion tracking. Magn Reson Med 1994; 31: 401-13.
13. Gudbjartsson, H, Patz, S. The Rician distribution of noisy MRI data. Magn Reson Med 1995; 34: 910-4.
14. Urkowitz, H: Signal Theory and Random Processes. In. Dedham, MA: Artech House, Inc., 1983; 452.
15. Stuber, M, Fischer, SE, Scheidegger, MB, Boesiger, P. Toward high-resolution myocardial tagging. Magn Reson Med 1999; 41: 639-43.
16. Stuber, M, Spiegel, MA, Fischer, SE, Scheidegger, MB, Danias, PG, Pedersen, EM, Boesiger, P. Single breath-hold slice-following CSPAMM myocardial tagging. Magma 1999; 9: 85-91.

Table 1. Scan Parameters

Parameter	Phantom #1	Phantom #2	Volunteer #1	Volunteer #2
TR (msec)	8.55	8.55	11.4	4.6
TE (msec)	4.2	4.2	2.6 fr	2.1
BW (kHz)	20.8	20.8	20.8	31.2
Flip Angle	10°	10°	10°	10°
FOV (mm)	250	280	280	280
Matrix	64 x 256	64 x 256	64 x 256	32 x128
Thickness (mm)	7	7	7	7
Phase Sample Ratio	1.0	1.0	1.25	1.0
Echo position	128 / 256	128 / 256	64 / 256	64 /128
R-R interval (msec)	1500	1500	1070	777
Trigger Window	30%	30%	20%	20%
PEG size (views per segment)	2	2	4	8
# of images	69	69	19	21
Temporal Resolution (msec)	17.1	17.1	45.6	36.8
Scan time / tag orientation (sec)	49	49	22	4
Tag cycle (mm)	8	28	6	6